Reducing Voltage Losses in Organic Photovoltaics Requires Interfacial Disorder Management

Rong Wang, *Leng Han, Ning Li, Christos L. Chochos, Vasilis G. Gregoriou, Larry Lüer,** *and Christoph J. Brabec**

Thanks to the introduction of non-fullerene acceptors, efficiencies of organic photovoltaics are now approaching 20%. Closing the gap with inorganic photovoltaics requires minimizing voltage losses without penalizing charge extraction, for which microstructure control is crucial. However, the complex interplay between microstructure and charge generation, recombination, and extraction has so far not been unraveled. Here, a systematic study linking device performance to distinct microstructural features via machine learning is presented. Building bi-layer devices allows to separately study the influence of aggregation and disorder on the energies and lifetimes of bulk and interfacial states. Unambiguous assignments of specific structural motifs to the device photophysics are thus possible. It is found that the control of aggregation-caused quenching is decisive for the exciton splitting efficiency and thus the carrier generation. Furthermore, the static disorder at the donor–acceptor interface controls the nonradiative recombination by shifting the excited state population from the bulk toward the interface. Finally, the amount of disorder in the bulk is found decisive for charge extraction. The finding that charge generation, recombination, and extraction are controlled by distinct structural features, is the key to optimizing these motifs independently, which will pave the way for organic photovoltaics toward the detailed balance limit.

1. Introduction

Organic solar cells (OSC) have seen a steep rise of power conversion efficiencies (PCE), now approaching 20%.[1,2] This is mainly due to the introduction of non-fullerene acceptors (NFA) reducing both the transmission losses, by broadening the optical absorption of the OSC, and the open circuit voltage (V_{oc}) losses, by reducing the "driving force" for exciton dissociation and charge separation. However, even in the highest-performing OSC, V_{oc} values still reach less than 75% of the detailed balance limit at the corresponding optical bandgap.[3–6] Therefore, tackling V_{oc} losses is currently the most promising handle for further increasing OSC performance, which requires a further reduction of the driving forces.

If the driving force for exciton dissociation is in the range of thermal energy, then exciton regeneration can take place, causing a dynamic equilibrium between localized excitons (LE) and charge transfer (CT) states. V_{oc} will thus be limited by electronic deactivation of both LE and CT states.[7] Under these conditions, there exist optimal driving forces for exciton dissociation (LE→CT) and for creation of charge separated states (CT→CS) which depend on both LE and CT lifetimes.[8,9] Taking these works together, minimizing V_{oc} losses boils down to three simple design rules: a) maximize LE and CT lifetimes, b) minimize the overall driving force (LE→CT→CS) and c) adjust the CT

R. Wang, L. Han, N. Li, L. Lüer, C. J. Brabec
Institute of Materials for Electronics and Energy Technology (i-MEET)
Friedrich-Alexander-Universität Erlangen-Nürnberg
Martensstrasse 7, 91058 Erlangen, Germany
E-mail: rong.w.wang@fau.de; larry.lueer@fau.de; christoph.brabec@fau.de
R. Wang
Erlangen Graduate School in Advanced Optical Technologies (SAOT)
Paul-Gordan-Straße 6, 91052 Erlangen, Germany

N. Li, C. J. Brabec
Helmholtz-Institute Erlangen-Nürnberg (HI-ERN)
Immerwahrstraße 2, 91058 Erlangen, Germany
N. Li
Institute of Polymer Optoelectronic Materials and Devices State Key
Laboratory of Luminescent Materials and Devices
South China University of Technology
Guangzhou 510640, P. R. China
C. L. Chochos, V. G. Gregoriou
Advent Technologies SA
Stadiou Street, Platani, Rio, Patras 26504, Greece
C. L. Chochos, V. G. Gregoriou
Institute of Chemical Biology
National Hellenic Research Foundation (NHRF)
48 Vassileos Constantinou Avenue, Athens 11635, Greece

ADVANCED
SCIENCE NEWS

www.advancedsciencenews.com

ADVANCED
ENERGY
MATERIALS

www.advenergymat.de

energy to its optimal value, providing maximum charge separation but at the same time allocating the unavoidable equilibrium population in {LE,CT} to the state of longer lifetime.

Karuthedath et al. have shown that the typical chemical structure of NFA, consisting of alternating electron-accepting and -donating moieties, can cause quadrupolar moments which can increase ionization energies (IE). As the effect is reduced at the donor–acceptor (D–A) interface, a driving force for charge separation results, overcoming Coulomb attraction in the CT states.[10] The price we pay is an increased overall driving force, which means that design rules (b) and (c) become entangled. Recently, Fu et al [11] have shown that within one and the same D–A blend, the amount of electrostatic stabilization critically depends on the processing conditions by virtue of controlling microstructure. However, the microstructure of the bulk and, in consequence, also of the D–A interface, has a crucial impact on the lifetimes of LE and CT states, respectively. Optimization of design rules (b) and (c) thus also becomes entangled with design rule (a).

Minimizing voltage losses in OSC requires disentangling design rules (a), (b), and (c). Ideally, one would hope for encountering orthogonal process conditions, selectively acting on either of these design rules. In reality, a more promising approach is to understand the effect of each available process condition on each of the design rules; this would allow an optimization procedure, finding a combination of process conditions yielding the desired values for (a), (b), and (c). To accomplish this, a selective and reliable characterization of the energies and lifetimes in the bulk and the D–A interface is mandatory, which is difficult in standard bulk heterojunction (BHJ) blends. For example, when calculating the exciton dissociation yield, intrinsic LE lifetimes are usually taken from pure acceptor films, an approach which obviously cannot be deployed when the focus of the study is the LE lifetime dependence on microstructure, to resolve the entanglement between (a) and (c). Bilayer device with an isolated D–A interface yields the possibility to "zoom in" on the local area of the D–A interface in the BHJ-OSCs. Sequential preparation of donor and acceptor layers allows to regulate the microstructure of each layer independently. This means that LE lifetimes can be reliably measured for each microstructure, and they are guaranteed to stay the same even after formation of the D:A interface. Moreover, verifying these design rules involves time-consuming experiments and expert interaction, which conflicts with the need of sampling a high-dimensional experimental space. To enable a high throughput workflow, appropriate proxy experiments need to be developed providing a rapid characterization of bulk and interfacial properties. The calibration of proxy experiments for microstructure-function relationships is strongly facilitated if we can rely on the microstructure – and the corresponding optical features – of the donor being unchanged. This is another argument for developing this method using bilayers formed by transfer printing.[12–14]

Here, we perform a comprehensive study on interfacial engineering by independently varying intermolecular interaction and disorder, which allows us to isolate their effects on charge generation, recombination, and extraction. We build bi-layer rather than bulk heterojunction devices by transferring a free-standing film of the donor polymer WF4 onto a spin-coated layer of the NFA molecule IT-4F (molecular structures shown in Figure S1, Supporting Information). Intermolecular interaction in the IT-4F phase is controlled by varying concentrations of a solid additive which is admixed to the solution for spin coating, while disorder is controlled by post-deposition annealing at various temperatures. The bilayer architecture allows us to thoroughly characterize the energetics and dynamics of LE states in the IT-4F bulk prior to formation of the D:A interface. Spectral modeling of UV–vis spectra is used to extract energetic and morphological features of the IT-4F bulk. Our method of film transfer ensures that subsequent formation of the D:A interface does not alter the properties of the IT-4F bulk. Characterizing the energetics and dynamics of the final bilayer devices, in comparison with the data from the IT-4F bulk, thus yields highly reliable values for the driving forces and transfer yields. We use Gaussian Process Regression (GPR) to establish the relationship between microstructural features and the decisive performance predictors, namely the exciton splitting efficiency (η_{exc}) nonradiative voltage losses ΔV_{oc}^{nr}, and the fill factor (FF). We find that these parameters are controlled to a large degree by specific microstructural features from bulk LE states to interfacial CT states. Since we also found a correlation between hard-to-measure interfacial properties and easy-to-measure optical probes, this will allow high throughput optimization in a larger dimensional experimental space.

2. Methods

The BL devices are composed of the medium band gap polymer donor (WF4) and the low-bandgap NFA IT-4F (chemical structures shown in Figure S1a,b, Supporting Information) to form the active layer. IT-4F has a typical A–D–A type sequence where A and D, refer to electron accepting and donating moieties, respectively.[15,16] IT4F exhibits an outstanding exciton diffusion length of >40 nm which is beneficial for use in bi-layer architectures, allowing to combine high light absorption and exciton dissociation yields.[17] The IT-4F films are prepared by spin coating from Chlorobenzene (CB) solutions. To explore the aggregation effect of NFA on the device performance, we introduce a solid additive (SA) into the solutions, namely SAA (chemical structure see Figure S1c (Supporting Information), which is structurally matched to the end group of IT-4F and therefore is supposed to intercalate in the solid-state.[18–20] Varying the solid additive concentration (c_{SA}) allows controlling the amount of intermolecular interaction in the IT-4F phase. Besides, applying post-deposition annealing at various temperatures T_a allows us to control the disorder in the IT-4F phase by removing the SAA at elevated temperatures.[24] Varying c_{SA} from 1:0 to 1:1.5, and T_a from 25 °C to 160 °C, we obtain 16 IT-4F layers with distinct morphologies. The expected effects on the IT-4F frontier orbitals are shown schematically in **Figure 1a**. Aggregation effects (mainly controlled by c_{SA}) will modify the optical bandgap, causing the IT-4F HOMO and LUMO energies to evolve in opposite directions (purple arrows). In contrast, electrostatic effects deriving from disorder, are expected to lead to a parallel evolution of HOMO and LUMO energies (orange arrows).[11] These effects are mainly controlled by T_a although a detailed analysis will show that the two process conditions are not fully orthogonal.

The BL solar cells (Figure 1b) were prepared by transferring WF4 films using on top of the IT-4F films by the spontaneous spreading transfer (SPT) method.[21,22] Since no dissolving agent is present during film transfer, an abrupt D:A interface is
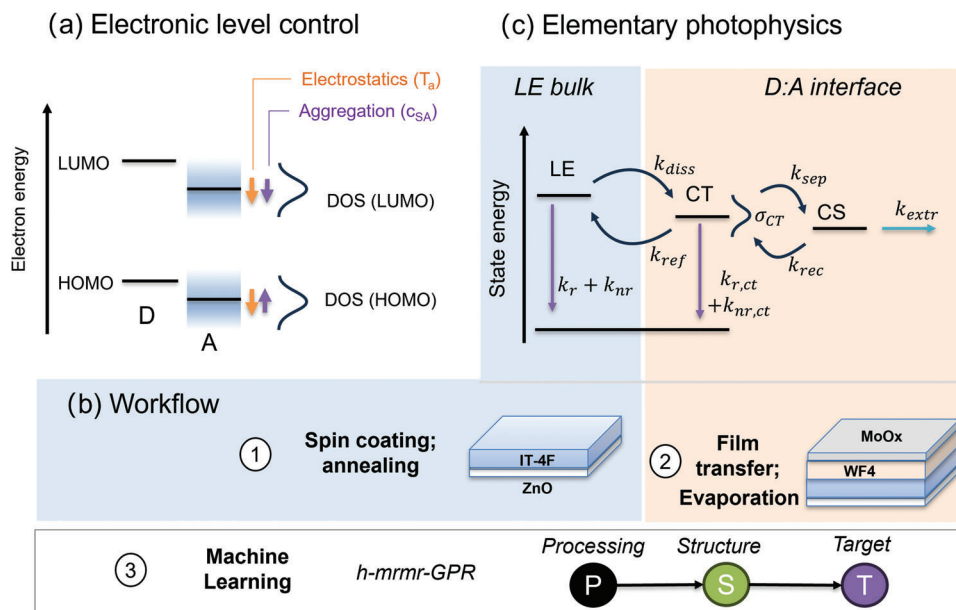
Figure 1. a) Schematic for electronic control by regulating NFA IT-4F processing conditions. b) The workflow from device prepare to data analysis. c) Photophysical properties at bulk and D–A interface, in which the aggregation of IT-4F control the kinetic equilibrium and energetic disorder. The degeneracy of the states is indicated by the line thickness.

obtained conserving the disorder adjusted by controlling the c_{SA} and T_a in the IT-4F phase, while the morphology in the WF4-phase is identical for all samples. The overall stack of BL-OSCs is an inverted device architecture with the layer sequence (ITO glass substrate/ZnO/IT-4F/WF4/MoOx/Ag), in which zinc oxide (ZnO) is the electron transport layer and molybdenum oxide (MoOx) is the hole transport layer. Figure 1b presents an overview of the workflow and Figure 1c sketches a simple rate equation scheme linking the process conditions to the design rules and finally to device performance. After photoexcitation of LE states and their diffusion to the D-A interface, exciton dissociation takes place, resulting in interfacial CT states that convert into charge separated states (CS) that can contribute to the photovoltaic effect. Note that being interfacial states, the degeneracy of CT states is much less than that of LE states (indicated as thickness of state lines). Both LE and CT states have radiative and non-radiative loss channels to the ground state; hence the balancing of the respective driving forces, and the relative stationary concentrations of LE and CT states under 1 sun illumination, will control the overall energy (voltage) and quantum (current) losses.[8,23] The driving force for exciton dissociation at the D–A interface ($\Delta E_{LE,CT}$) is defined by the Gibbs energy difference between the localized exciton (LE) of the material with the lowest bandgap (here, IT-4F) and the energy of the interfacial CT state[24]:

$$\Delta E_{(LE,CT)} = E_{LE}^{IT-4F} - E_{CT} \tag{1}$$

The driving force for charge separation is given by the difference between E_{CT} and the effective gap E_g of the charge separated (CS) state,

$$\Delta E_{CT,CS} = E_{g,eff} - \Delta E_{LE,CT} \tag{2}$$

where the effective gap is given by the energy offset between the lowest unoccupied molecular orbital (LUMO) of the acceptor and the highest occupied molecular orbital (HOMO) of the donor:

$$E_{g,eff} = E_{LUMO}^A - E_{HOMO}^D \tag{3}$$

CS states, being in their electronic ground state, can only disappear through recombination into CT states or through extraction into the outer electric circuit. For simplicity, both pathways are assumed as first-order rate constants k_{rec} and k_{extr}, respectively. In contrast, both LE and CT states are electronically excited states with the respective radiative (r) and non-radiative (nr) deactivation pathways, see downward arrows in Figure 1c.[25]

The results part is organized as follows: in Part 1, we identify trends in the device performance upon variation of c_{SA} and T_a, identifying the optimal process conditions for maximum PCE. In Part 2, we characterize the energetics and dynamics of bulk LE states by looking at the IT-4F films before deposition of the donor polymer. In Part 3, we characterize the CT states at the D–A interface in IT-4F:WF4 bilayers and show the critical influence of disorder. We encounter fast proxy experiments enabling high throughput workflows and allowing a transfer of the method to BHJ devices. In part 4, we introduce a machine learning workflow to identify decisive structural features controlling electrical performance, yielding processing – structure – performance relationships for disorder management at the D:A interface.

3. Results

3.1. Electrical Performance

In **Figure 2a**, we show current–voltage ($J–V$) characteristics for different c_{SA} values, with $T_a = 25$ °C. We find that the presence
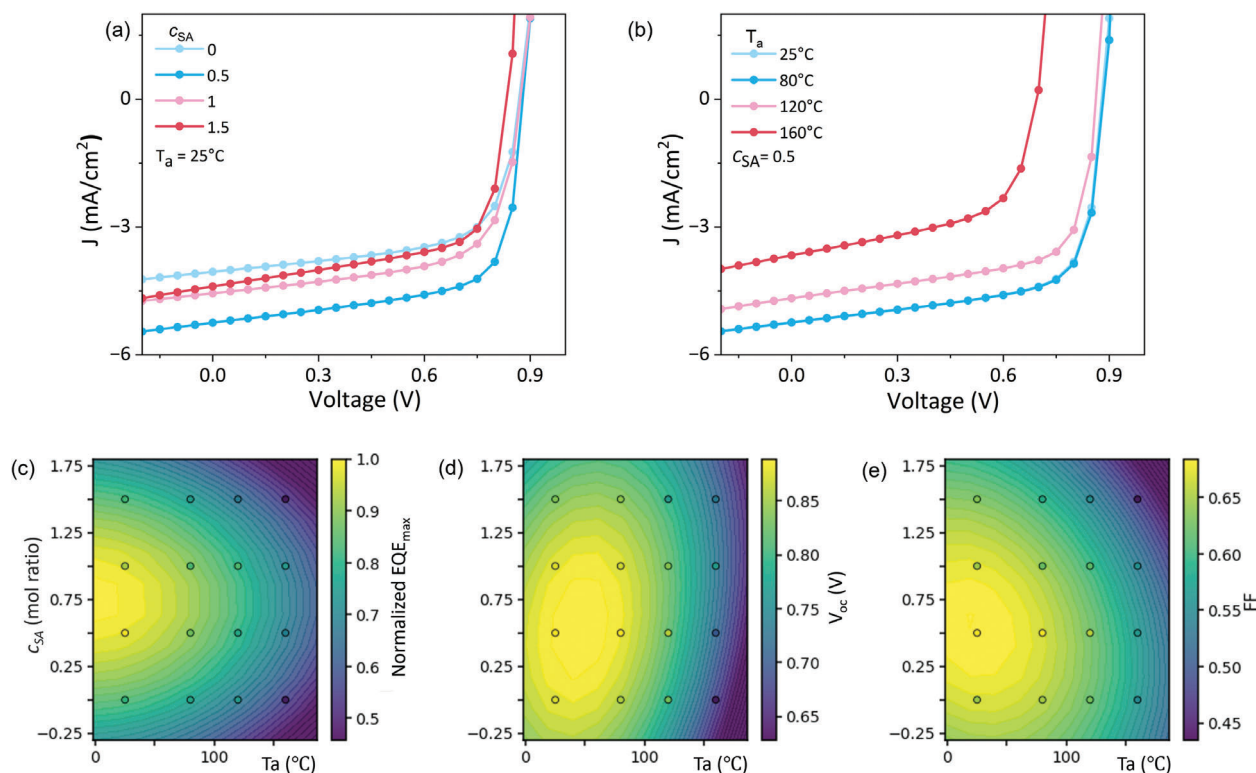
Figure 2. a,b) $J–V$ curves characterization in BL devices with different molar ratios of solid additive c_{SA} and post-annealing temperature T_a, under 1 sun illumination, AM 1.5 G, 100 mW cm^{-2}. c–e) 2-D contour plots of 16 different processing conditions and device parameters normalized EQE_{max}, V_{oc}, and FF.

of SAA leads to a strong increase of the short-circuit current J_{sc}, the effect being maximum for $c_{SA} = 0.5:1$. In contrast, V_{oc} values are only weakly increased upon introduction of small SAA concentrations, compare dark blue and light blue curves for $c_{SA} = 0.5:1$ and 1:1, respectively. In Figure 2b, we show $J–V$ characteristics for different T_a values, keeping c_{SA} at its optimal value ($c_{SA} = 0.5:1$). For $T_a = 80$ °C, a small increase of V_{oc} is observed, and J_{sc} remains unchanged compared to $T_a = 25$ °C, compare light blue and dark blue curves, respectively. For higher annealing temperatures, a strongly detrimental effect is observed on both J_{sc} and V_{oc} values. More details about device performance are shown in Figures S2–S5, and Table S1 (Supporting Information).

Figure 2c–e presents the normalized external quantum efficiency (EQE_{max}), V_{oc}, and FF as function of c_{SA} and T_a, representing their effect on charge generation, recombination, and extraction, respectively (data points). We use Gaussian Process Regression (GPR, a non-parametric multidimensional interpolation method) to show the trends more clearly in the form of false color hypersurfaces. The high fidelity of the GPR predictions is shown by the fact that data points and hypersurface have identical colors; (see also result plots in Figure S2, Supporting Information in the ESI). Figure 2c shows that the EQE_{max} is strongly influenced by both c_{SA} and T_a, with a maximum around $c_{SA} = 0.5–1$ at RT. Any increase of the annealing temperature leads to a strong reduction of normalized EQE_{max} below 85%. In contrast, the V_{oc} (Figure 2d) is less sensitive to changes of c_{SA} and T_a, retaining values above 0.85 V even at $T_a = 80$ °C and for c_{SA} between 0 and 1. Only for $T_a \geq 120$ °C, a sharp decrease of V_{oc} is

observed. Figure 2e shows that in order to obtain a high FF, both solid additive concentration and annealing temperature should be low. From the dark $J–V$ curves of BL-OSCs as shown in Figure S6 (Supporting Information), we know that the recombination-related ideality factor (n) and the shunt resistance are sensitive to both c_{SA} and T_a. Importantly, the same trends for V_{oc} are obtained for bulk heterojunction samples, as plotted in Figures S7 and S8 and Table S2 (Supporting Information), which is a common phenomenon in ITIC-type and Y6-type based BHJ-OSCs.[26,27] This shows that the BL devices represent a valid model system to understand voltage losses in BHJ samples. While the J_{sc} shows an opposite dependence, it can be attributed to the amount of D–A interface and the change in WF4 aggregation after annealing. These highly reliable trends show that the chosen process conditions have a distinct influence on exciton dissociation, recombination, and extraction, which should allow us to disentangle their influence on the underlying physics. In particular, they confirm that the solid additive SAA, when added in small concentrations, has a beneficial effect on both free charge generation and V_{oc}.

3.2. Characterization of the IT-4F Bulk: Aggregation Induced Quenching and Disorder

Photophysical properties of the solid state decisively depend on the type of packing. Aggregation of organic semiconductors is usually described in terms of H- or J-aggregation, strongly influencing the radiative and nonradiative exciton decay rate

**ADVANCED
SCIENCE NEWS**

www.advancedsciencenews.com

**ADVANCED
ENERGY
MATERIALS**

www.advenergymat.de

constants.[28,29] Since IT-4F exhibits an acceptor–donor–acceptor (A–D–A) structure, the preferred alignment is the head-to-tail (A–A) J-aggregation type, which however can be influenced by process conditions.[30,31] The morphology of the IT-4F phase was characterized by the UV–vis absorption, while the LE decay processes were analyzed by steady-state and time-resolved photoluminescence (PL and TRPL) spectra, as shown in **Figure 3a–c** and Figures S9–S16 (Supporting Information). In Figure 3a we show normalized UV–vis spectra of pure IT-4F films for different values of T_a and c_{SA} (left and right panel in Figure 3a, respectively). Increasing T_a leads to a red shift of the excitonic absorption band, a sign of formation of extended J aggregates, and to an increase of the absorption for wavelengths <620 nm, an indication for an increased contribution from the amorphous (disordered) phase. Upon changing the SAA mixing ratio, only small spectral changes are observed in the region of the vibronic (0–1) transition at 1.9 eV.

Figure 3b shows the evolution of PL spectral intensity with the process conditions. We find a monotonous increase of PL intensity with c_{SA}, while increase of T_a reduces the PL intensity. In order to distinguish whether c_{SA} and T_a control radiative or non-radiative pathways of LE recombination, we measure time-resolved photoluminescence (TRPL), where the effective exciton lifetime $\tau = (k_r + k_{nr})^{-1}$ is obtained.[32] Figure 3c shows that an increase of T_a reduces τ while an increase of the SA concentration increases τ. Taking the information from steady-state PL and TRPL together, we can get k_r and k_{nr} for each sample, see Figure 3e,f, respectively. We find that increasing c_{SA} increases k_r, but only if $T_a < 100\,°C$. Since we know that SAA leaves the sample at higher annealing temperatures, this means that the increase of k_r is caused by the presence of the solid additive in the samples. Increasing the annealing temperature reduces k_r, which is explained by the loss of SAA.

This explanation is supported by the sharp decrease of the acceptor exciton energy c_1 for the highest annealing temperature, see Figure S15 (Supporting Information). The nonradiative recombination constant k_{nr} decreases for increasing c_{SA} for unannealed samples, see Figure 3c,f. This observation speaks for a planarization of the IT-4F backbone induced by the presence of SAA, which would also explain the concomitant increase of k_r. In the absence of SAA, the annealing temperature T_a has no influence on k_{nr}, whereas a strong increase of k_{nr} is found for increasing T_a if $c_{SA} > 0$. This observation is an indication that the process of SAA evaporation at elevated temperatures induces structural changes in the sample leading to enhanced internal conversion. This notion is confirmed by a steep increase of the amount of amorphous phase χ_{amA}, for $T_a > 80\,°C$, see Figure 3d. Here, the relative amount of the amorphous phase is defined as $\chi_{amA} = A_{1,ord}/(A_{1,ord} + A_{1,am})$, where $A_{1,ord}$ and $A_{1,am}$ are the total spectral integrals of the lowest energetic UV–vis absorption bands from the ordered and amorphous regions, respectively. A detailed description of the morphological features can be found in Figure S10 and Table S3 (Supporting Information).

For low molar ratios of SAA ($c_{SA} = 0.5:1$) we observe a reduction of χ_{amA} together with an increase of the exciton energy c_1 (Figure S15, Supporting Information). This observation confirms the notion that introduction of SAA reduces aggregation and at the same time leads to higher ordering. For higher SAA concentrations, the increased SAA ratio results in the growth of χ_{amA}

and a redshift of c_1. This increase in χ_{amA} is accompanied by a reduction of relative PLQY and an increase of the nonradiative rate constant k_{nr}, see Figure 3e,f, respectively. It is worth noting that in the absence of SAA, k_{nr} maintains a stable value at different annealing temperature, see red curve in Figure 3f.

The optical bandgaps of the IT-4F films range from 1.596 to 1.630 eV, as determined from the crossing point of absorption and emission spectra shown in Figures S11–S14 (Supporting Information). An obvious redshift of the absorption edge and maximum of the 0–0 vibronic progression is shown in Figure 3a. Comparing the energetic offset of the 0–0 transitions of UV–vis and PL spectra, we obtain the Stokes shift E_{st} as plotted in Figure S16f and Table S3 (Supporting Information), which is found in a range from 0.081 to 0.148 eV. The Stokes shift represents the thermal energy loss of the first excited states by vibrational relaxation. In our dataset, E_{st} is reduced together with c_1, that is, with the amount of J aggregation.[33,34] Using these features, we find that the E_{st} is highly relevant to k_{nr} (Figure S16, Supporting Information). For intermediate SAA concentrations and highest annealing temperatures, the smallest E_{st} values are found, leading to the highest k_{nr} values of all samples.

The energy gap law links the nonradiative decay rate constant k_{nr} with the energy difference ΔE of the electronic states between which internal conversion occurs.[32,35,36]

$$k_{nr} = a\,e^{-\gamma\,\Delta E} \tag{4}$$

where γ refers to the highest energy vibrational mode involved in the non-radiative transition, ΔE is the energy difference between GS and lowest LE states, and a is a proportionality constant. According to Equation (4), exciton lifetime in OSCs can be increased by suppressing the internal conversion.[37]

3.3. Characterization of the D:A Interface: Driving Forces, Dynamics, and Disorder

Normalized FTPS-EQE spectra are shown in **Figure 4a**. In the upper panel, the evolution of the spectral shapes with T_a is displayed, exhibiting little change as long as $T_a \leq 120\,°C$. For $T_a = 160\,°C$, a clear red shift of the main absorption band is encountered, in agreement with the data in Figure 3a, left panel. Moreover, we observe a pronounced shoulder at lower energies, representing absorption from the CT state. In the lower panel, the evolution of the spectral shapes with c_{SA} is displayed, showing a blue shift as c_{SA} is increased.

Figure 4b shows normalized EL spectra, exhibiting clear shoulders at ≈1.4 eV, ascribed to CT emission, besides the EL maxima at ≈1.56 eV due to emission of LE states in Boltzmann equilibrium with the CT states created by interfacial recombination of the injected charges. A comparison with PL spectra in neat IT-4F (Figure 3b) shows that part of the signal at 1.4 eV in the EL spectra could also be due to the (1–0) vibronic replica. However, clear processing-dependent spectral shifts and strong intensity variations in Figure 4b speak for dominance of EL from the CT state. We find that increasing T_a increases the intensity of the shoulder at 1.4 eV and shifts it to blue, see upper panel in Figure 4b. As shown in the lower panel of Figure 4b, the presence of SAA generally shifts the shoulder at 1.4 eV to the red. A particularly low
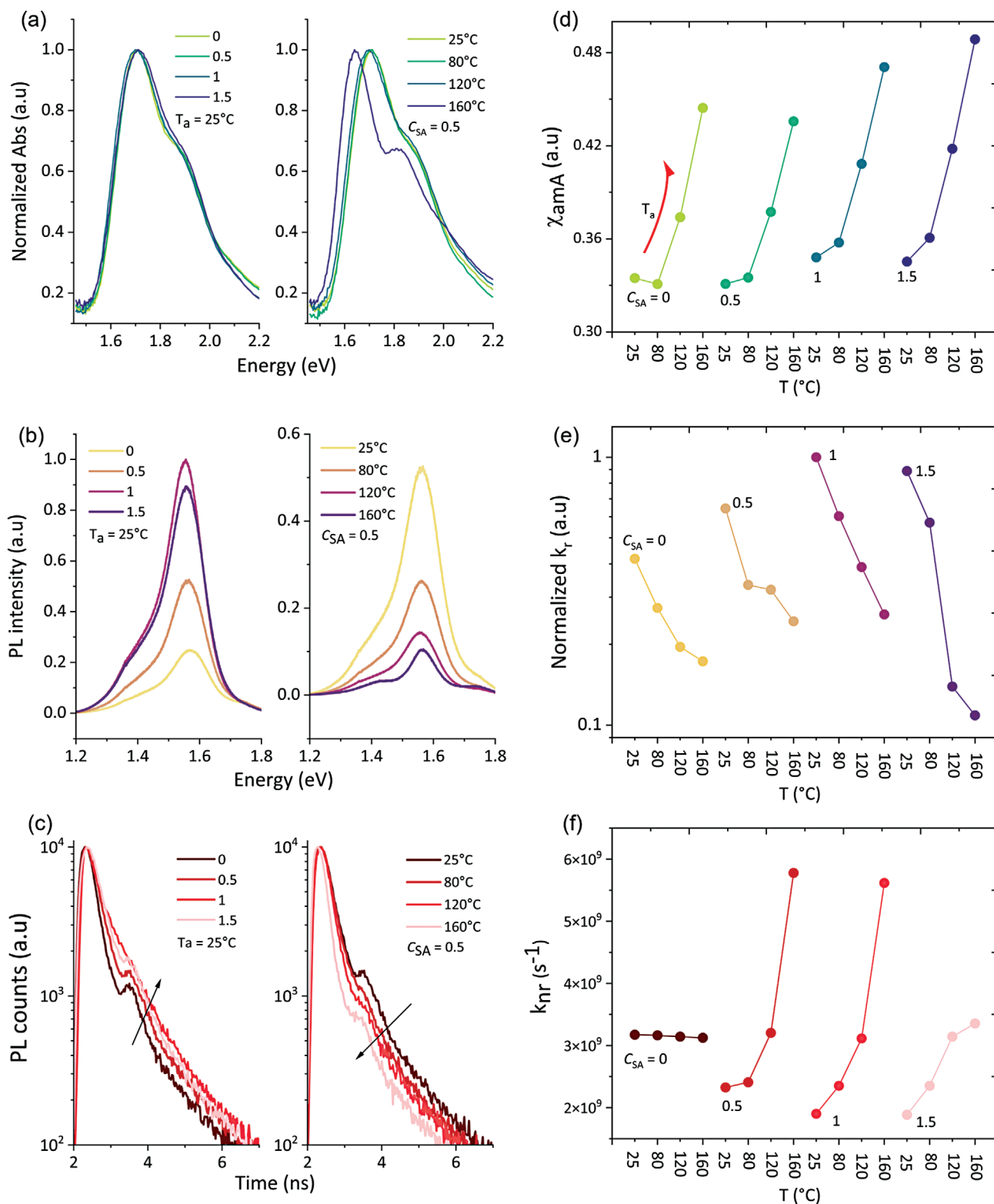
Figure 3. a–c) Absorption, PL emission, and time-resolved PL decay of neat IT-4F films, which are present two opposite evolution by post-annealing and solid additive. d–f) Processing induced the variation of amorphous ratio, PL quenching, and the exciton nonradiative decay in neat IT-4F films. Here, 0-RT indicates that the film was processed without SAA at room temperature, 0.5, 1, and 1.5 indicate the increase in SAA molar ratio. T80, T120, and T160 mean that the film was post-annealed at 80 °C, 120 °C, and 160 °C respectively.

ADVANCED
SCIENCE NEWS

www.advancedsciencenews.com

ADVANCED
ENERGY
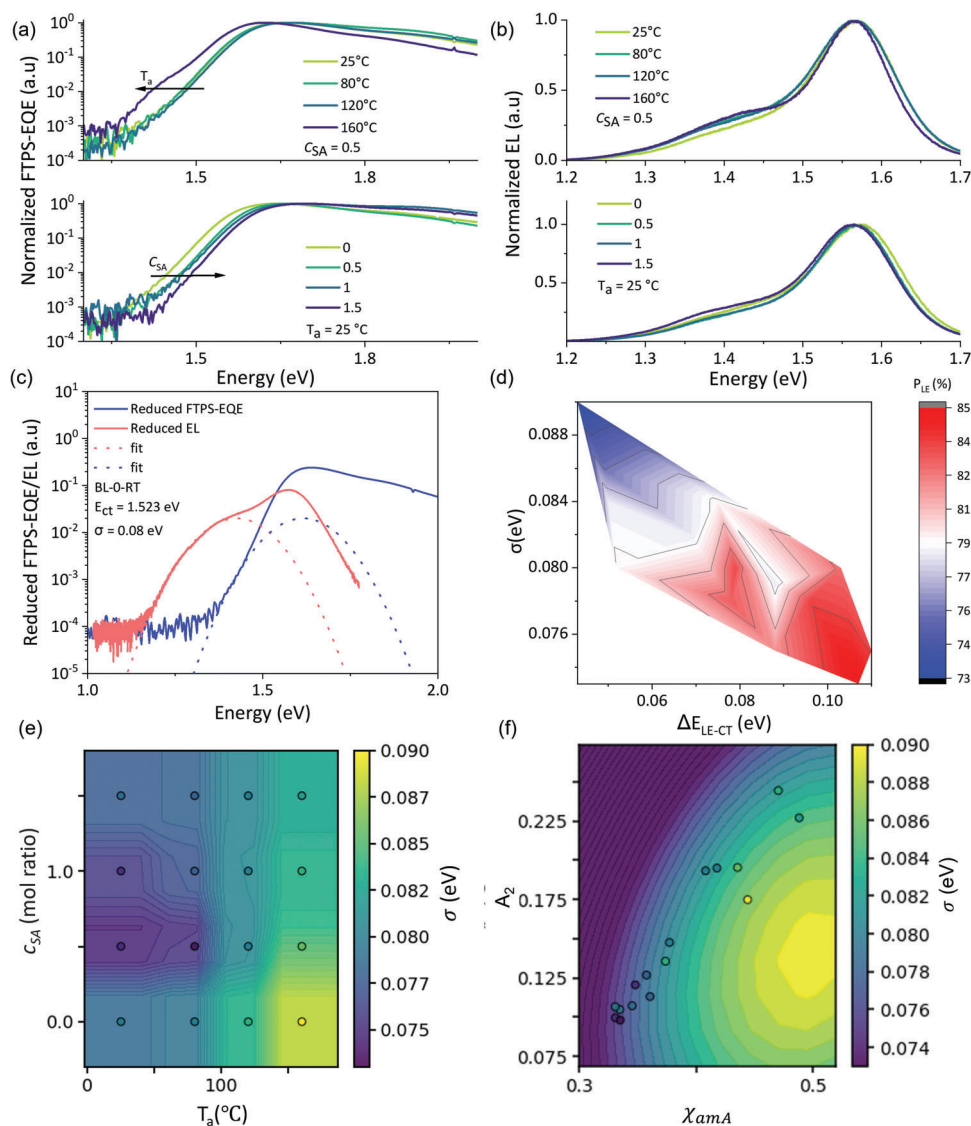**MATERIALS**

www.advenergymat.de

Figure 4. a,b) Normalized absorption and emission of CT states as function of the processing parameters c_{SA} and T_a. c) Determination of value and width of CT states by bi-Gaussian fitting of FTPS-EQE and EL spectra. d) Relative population of LE states P_{LE} (color-coded, see color bar) as function of driving force for exciton dissociation (ΔE_{LE-CT}) and interfacial energy disorder (σ_{CT}). e) Control of interfacial energy disorder by processing conditions. (c) Prediction of interfacial energy disorder by features from the UV–vis spectrum.

intensity of the shoulder, relative to the main EL peak, is found at $c_{SA} = 0.5$:1 which means that at this SAA concentration, where our BL devices show best performance, the emission from the CT state is suppressed to the favor of emission from the LE state.

These qualitative findings are confirmed by obtaining values for E_{CT} and σ, which is accomplished by fitting both EL and FTPS-EQE spectra with a single Gaussian line shape for each spectrum,[38,39] allowing different energetic positions and relative heights, but requiring the same width; an example is shown in Figure 4c; the complete set of data is shown in Figures S17–S20 (Supporting Information). We obtain E_{CT} as the intersection between both normalized Gaussian bands. Comparing E_{CT} with E_{LE}, we obtain the driving force for exciton dissociation ΔE_{LE-CT}. As predicted from visual inspection of Figure 4b, ΔE_{LE-CT} is maximum for $c_{SA} = 0.5$:1 at room temperature, reaching 0.11 eV

(see Figures S21 and S22 and Table S5, Supporting Information) which is more than two times the thermal energy k_BT at room temperature. To quantify interfacial disorder, we obtained spectral widths σ in the range from 0.073 to 0.090 eV. The lowest disorder for the interfacial CT state σ is found for an SAA molar fraction of = 0.5:1 at T_a between 25 °C and 80 °C, see Figure 4e, which coincides with the highest V_{oc} values in Figure 2b. This shows that low energetic disorder of interfacial CT states is decisive for electric performance.[12,40–42]

In order to quantify the dynamic equilibrium between LE and CT states for OSCs with small ΔE_{LE-CT}, we calculate the relative population of LE, given as $r(LE) = p(LE)/(p(LE) + p(CT))$, where p(LE) and p(CT) are the populations of excited LE and CT states, respectively.[43] The detailed procedure is given in the Supporting Information, part 3. In Figure 4d, we display the
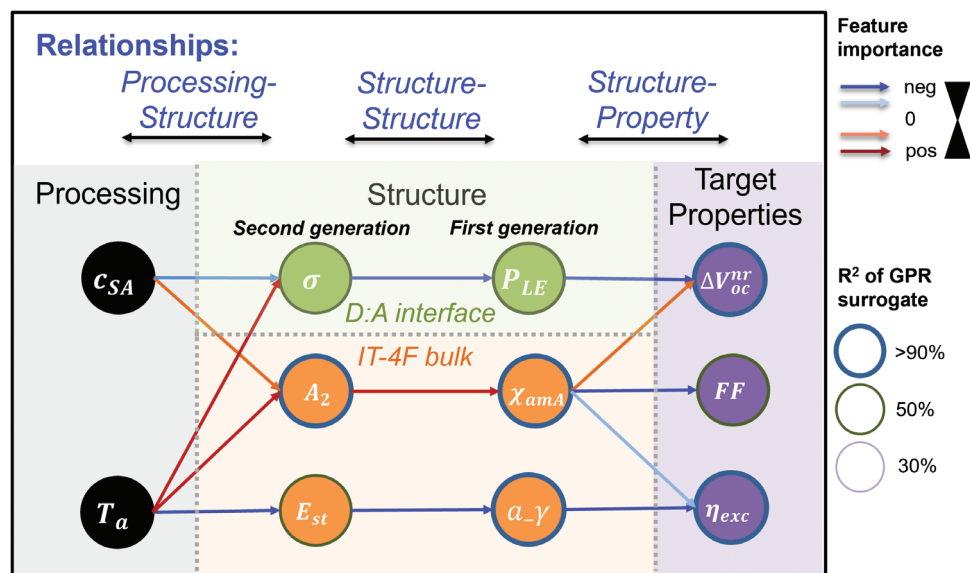
**ADVANCED
SCIENCE NEWS**

www.advancedsciencenews.com

**ADVANCED
ENERGY
MATERIALS**

www.advenergymat.de

Figure 5. a) Knowledge graph for the prediction of target properties (purple) from structural features (green for interface, orange for IT-4F bulk) and from processing conditions (black), as obtained by hierarchical minimum Redundancy Maximum Relevance embedded Gaussian Process Regression (h-mrmr-GPR). Each node represents the target of an individual mrmr-GPR run, with the in-edges as relevant and non-redundant predictors (color of arrows indicates feature importance). The colors of edges refer to feature importance, and line width of nodes refers to R2 value for GPR surrogate model, see legend on the right.

calculated r(LE) values on a false color scale as function of the driving force ΔE_{LE-CT} and the interfacial disorder σ. (Values also given in Table S5, Supporting Information). Strikingly, we observe highest values for r(LE) when ΔE_{LE-CT} is high. In a Boltzmann equilibrium picture, one would expect the opposite trend, namely an accumulation of population on CT states and thus low r(LE) values if driving forces are high. In a simple two – state model,[7] the observation in Figure 4d can be explained by a higher degeneracy ratio between LE and CT states as the driving force increases, keeping the average population on the LE states despite the increase of driving force.[7,9] Furthermore, Figure 4d shows that static disorder increases as the driving force decreases, which is correlated with a shift of population toward the CT state, which can be seen by the evolution of the color scale from red to blue along the vertical direction for fixed values of ΔE_{LE-CT}. It has been reported that a higher LE population in equilibrium is associated with the reduction of nonradiative recombination loss.[44]

In our BL devices, we have introduced a variation of interfacial disorder σ by adjusting the microstructure in the IT-4F phase. These phenomena should therefore be related. Figure 4f shows that the interfacial disorder σ can be predicted with high accuracy from considering two features from the UV–vis spectra: The relative amount of amorphous phase (χ_{amA}) and the relative strength of the second lowest allowed electronic transition (A_2), a measure for the excitonic persistence length.[45] Both correlations make sense from a physics point of view, since both increased torsional freedom (measured by χ_{amA}) and the presence of rotamers (reducing the persistence length and thus increasing A_2) lead to a larger structural variation at the IT-4F interface, explaining the increase of σ. Importantly, both χ_{amA} and A_2 are obtained by a simple UV–vis measurement followed by automated feature extraction. Thus, the surrogate model (colored hypersurface in

Figure 4f defines a fast proxy experiment, allowing the prediction – and autonomous optimization – of interfacial disorder in a high-throughput workflow.

3.4. Management of Disorder: A Knowledge Graph Approach

In the previous two sections, we have shown that changing T_a and c_{SA} has significant effects on dynamics, energetics, and disorder, both in the IT-4F bulk and at the interface with WF4. For a comprehensive picture, we need to understand i) the importance of these effects for the electrical performance, ii) their link with microstructure, and iii) the extent to which we can individually control them by processing. In the following, we accomplish these tasks by a novel workflow, which we name hierarchical minimum Redundancy Maximum Relevance embedded Gaussian Process Regression (h-mrmr-GPR). It is essentially a recursive application of mrmr-GPR as introduced by Liu et al.[46] The result is shown in **Figure 5**, where the algorithm works from right to left. Out of all evidence collected in the previous two sections, the method first identifies the relevant and non-redundant structural predictors (green/orange region in Figure 5) for each of the chosen target properties (purple region), yielding structure-property relationships. If the explanation of variance (shown as line thickness of the nodes) is high, then these predictors must convey the essential information about the underlying device physics. In the next step, these essential (first generation) predictors are used as targets in another mrmr-GPR run, identifying structure–structure relationships toward the remaining structural predictors of the dataset. These structure–structure relationships allow detailed microstructural assessments such as distinguishing electronic from electrostatic interactions (see below). In the last step, we quantify to which extend these second-generation

structural predictors can be controlled by the available process conditions (gray region in Figure 5); this is accomplished by individual GPR runs with c_{SA} and T_a as fixed set of predictors. Experimental results, calculations, and GPR results as shown in Figures S23–S35 (Supporting Information).

Figure 5 shows that the nonradiative voltage losses ΔV_{oc}^{nr} are controlled mainly by the relative amount P_{LE} of excited state population in the LE state and thus by the Boltzmann equilibrium. This result agrees with ref. [7] and confirms the importance of the adjustment of the equilibrium population to reduce voltage losses. However, the structure–structure relationships (green region in Figure 5) strikingly show that in the present dataset, this adjustment is not accomplished by controlling the driving force $\Delta E_{LE,CT}$ as one would expect; instead, the only relevant structural predictor for P_{LE} is found to be the interfacial disorder σ. Although the chosen process conditions allow variation of $\Delta E_{LE,CT}$ by >60 meV (see Figure 4d), the effect of $\Delta E_{LE,CT}$ on the redistribution of the equilibrium population in LE and CT is completely overwhelmed by the concomitant variation of interfacial disorder. As shown in Figure 4d, disorder can even lead to a reversal of the population trend with driving force, increasing the LE population when increasing the driving force. Considering the photophysical scheme in Figure 1c, this reversal may be caused by an entropic effect, increasing the degeneracy of CT states if σ attains high values. This clearly highlights the importance of considering disorder when optimizing driving forces by means of process parameter variation. As shown in Figure 5, introduction of solid additives reduces σ (see blue arrow from c_{SA} to σ), while increase of the annealing temperature T_a strongly increases σ (red arrow from T_a to σ). Therefore, Figure 5 confirms that the main reason for the reduction of voltage losses by SAA is reduced interfacial disorder.

Turning now to the fill factor, we identify the amount of amorphous phase in the IT-4F bulk (χ_{amA}) as the only relevant predictor. This is plausible because in extended amorphous phases, the charge extraction mobility is expected to be smaller than in ordered domains. Again, structure–structure relationships yield additional insight into structural details. The strongest structural predictor for χ_{amA} is A_2, the relative strength of the second lowest energetic optical transition in IT-4F. This predictor refers to average chromophore length defining the persistence length of the excitonic wavefunction.[45] Higher persistence lengths increase the oscillator strength of the low energetic exciton transition on the expense of the higher energetic ones, such that a higher persistence length should lead to lower A_2. The strong correlation between χ_{amA} and A_2 suggests a significant reduction of the effective conjugation length of the individual IT-4F molecules in the amorphous phase compared to the ordered phase, for example by isomerization or torsion.

Finally, we turn to the exciton dissociation yield η_{exc}. We find that the parameter $a.\gamma$ related to $\ln(k_{nr})/E_{LE}$, derived from Equation (4), is the most important predictor for η_{exc}. In the supporting information (Figures S33 and S34, Supporting Information) we show that without $\ln(k_{nr})/E_{LE}$, as predictor, the algorithm chooses k_{nr} and A_2, a predictor for the persistence length, as essential predictors for η_{exc}. As the persistence length is related to torsional freedom and/or the presence of rotamers, this points to the importance of dynamic disorder for exciton dissociation.[45] This observation shows that $\ln(k_{nr})/E_{LE}$ contains more relevant physics for exciton dissociation than k_{nr}, essentially reporting only the bulk exciton lifetime. Indeed, in the structure–structure relationships, we find the Stokes shift E_{st} as the only relevant predictor for $\ln(k_{nr})/E_{LE}$, explaining >90% of its variance. J aggregation reduces vibrational disorder thereby reducing the Stokes shift.[45] The connection between E_{st} and $a.\gamma$ in Figure 5 can be explained by recent quantum chemical results by Wang et al.,[47] showing that if the excitonic coupling exceeds about half of the molecular reorganization energy, then the effect of the Energy Gap Law becomes dominating, leading to an increase of k_{nr} causing a reduction in η_{exc}.

4. Conclusion

In this work, we have presented a detailed study of the link between solid state morphology and electrical performance in organic photovoltaics. We have used bi-layer photovoltaic devices of the non-fullerene acceptor IT-4F and the donor polymer WF4 to study the link between IT-4F bulk microstructure and the properties of the donor–acceptor interface. It's found that admixture of a structurally matched solid additive to the IT-4F improves charge extraction and decreases voltage losses. This beneficial effect on device performance was explained by an increase of radiative deactivation and a suppression of nonradiative deactivation, probably due to a planarization effect exerted by the solid additives. This was corroborated by a reduction of bulk disorder, as observed by morphology sensitive features from UV–vis spectra. In contrast, increasing the annealing temperature resulted in an increase of bulk disorder and a concomitant reduction of device performance.

We showed that bulk disorder in the IT-4F phase leads to static energy disorder of interfacial charge transfer states. Using machine learning to identify essential predictors for microstructure and performance, we found that interfacial disorder is the decisive cause for voltage losses, even overwhelming the known effect of the driving forces. An optimum solid additive concentration of 0.5:1, where interfacial disorder is minimum, corresponds to minimum voltage losses. We further found that reducing bulk disorder is decisive for maximizing the fill factor, and that low dynamic disorder (electron-vibrational coupling) is crucial for maximizing exciton dissociation. These findings highlight that different aspects of disorder control losses in voltage, current or fill factor, which means that different motifs of chemical structure and processing conditions may be used for their selective optimization. This is an important step toward achieving orthogonal control of electrical performance aspects, avoiding Pareto frontiers where one aspect can only be optimized upon compromising others. Using machine learning, we also found a surrogate model for predicting hard-to-measure interfacial disorder from easy-to-measure aspects of bulk disorder. This will allow physics-aware optimization of process conditions in an autonomous high throughput workflow.

5. Experimental Section

Materials: ZnO-N10 was provided by Avantama AG. IT-4F and SAA were purchased from on Solarmer Energy, Inc. WF4 was synthesized by Advent Technologies Inc.

**ADVANCED
SCIENCE NEWS**

www.advancedsciencenews.com

**ADVANCED
ENERGY
MATERIALS**

www.advenergymat.de

Device Fabrication: At first, ITO glass substrates were ultrasonic cleaned for 15 min by deionized water, acetone, and isopropanol sequentially. Then 30 nm electron transport layer ZnO was deposited by spin-coater and annealed 15 min at 200 °C The active layers of BHJ-OSCs were spin-coated based on WF4:IT-4F solutions in CB at 10 mg mL^{-1}, weight ratio is 1:1. As for BL devices, the concentration of pure IT-4F solution was 10mg mL^{-1} in CB at room temperature and deposited by spin-coater at 2000 rpm, and post-annealed at RT, 80 °C, 120 °C, and 160 °C 10 min. Four different SAA molar ratios (1:0, 1:0.5, 1:1, and 1:1.5) were added into IT-4F solutions. Then the polymer donor films were transferred on the top of the IT-4F without annealing. The polymer solution was prepared in CB at 10 mg mL^{-1} over 5 h at room temperature and drop 10 μL solution onto the water surface of a 3 cm petri dish. The polymer film could be formed by spontaneously spreading as the reference. Only the process of IT-4F films was changed and keep the donor with the same conditions. Lastly, all the samples were transferred into the glove box, 10 nm hole transport layer MoOx and 100 nm electrode Ag were evaporated successively in a vacuum of ≈10^{-6} mbar.

J–V Measurement: All the devices with 0.104 cm^{-2} effective area and the J–V curves were measured by Keysight B2901 A under AM 1.5G solar spectra at 100 mW.cm^{-2}, which was provided by solar simulator Oriel Sol 1A; Newport.

UV–vis Absorption and Steady PL: The UV–vis absorption spectra for samples were measured by i-HR-320 monochromator, Horiba. Steady PL spectra were detected by a silicon charge-coupled device detector and a InGaAs detector, where the samples were excited by a 402 nm laser and detected at a range from 650 to 1200 nm.

TRPL: The TRPL measurements were conducted by the Fluotime 300 from Picoquant, where the plused laser was 402 nm for exciting polymer donor's acceptor. The emission signal of samples was then detected by a single-photon-counting PMT detector. EasyTau 2 internal software was used to fit the measured data to get the exciton lifetime (neat films) and PL quenching time (BL films).

EQE, EL, and FTPS-EQE Measurement: Quantum efficiency measurement system QE-R (Enlitech) was used to record the EQE data for all the samples. EL measurements were conducted by applying a forward voltage to the devices. The luminescence spectra were dispersed by iHR-320 monochromator (Horiba) and recorded by a Peliter-cooled Si CCD and liquid-nitrogen-cooled InGaAs detector (Horiba). The Brucker Vertex 70 Fourier-Transform infrared (FTIR) spectrometer performed the FTPS measurements. It was equipped with a low-noise current amplifier (Femto DLPCA-200) for amplifying the photocurrent signal. Then the data obtained from FTIR spectrometer were corrected by the EQE data measured from QE-R (Enlitech).

Supporting Information

Supporting Information is available from the Wiley Online Library or from the author.

Acknowledgements

Conflict of Interest

The authors declare no conflict of interest.

Author Contributions

R.W. proposed the experiment plan and conducted data analysis. L.H. performed the sample preparation and optical characterization of neat IT-4F films. N.L. provided the help of electrical data analysis and constructive of the manuscript. C.L.C. and V.G.G. synthesized the polymer donor WF4. L.L. developed the model for morphology features extraction and GPR prediction. C.J.B. directed the work.

Data Availability Statement

The data that support the findings of this study are available in the supplementary material of this article.

Keywords

[1] L. Zhu, M. Zhang, J. Xu, C. Li, J. Yan, G. Zhou, W. Zhong, T. Hao, J. Song, X. Xue, Z. Zhou, R. Zeng, H. Zhu, C.-C. Chen, R. C. I. MacKenzie, Y. Zou, J. Nelson, Y. Zhang, Y. Sun, F. Liu, *Nat. Mater.* **2022**, *21*, 656.

[2] S. Luo, C. Li, J. Zhang, X. Zou, H. Zhao, K. Ding, H. Huang, J. Song, J. Yi, H. Yu, K. S. Wong, G. Zhang, H. Ade, W. Ma, H. Hu, Y. Sun, H. Yan, *Nat. Commun.* **2023**, *14*, 6964.

[3] M. Azzouzi, T. Kirchartz, J. Nelson, *Trends Chem.* **2019**, *1*, 49.

[4] S. M. Menke, N. A. Ran, G. C. Bazan, R. H. Friend, *Joule.* **2018**, *2*, 25.

[5] S. Liu, J. Yuan, W. Deng, M. Luo, Y. Xie, Q. Liang, Y. Zou, Z. He, H. Wu, Y. Cao, *Nat. Photonics.* **2020**, *14*, 300.

[6] J. Zhou, D. Li, L. Wang, X. Zhang, N. Deng, C. Guo, C. Chen, Z. Gan, C. Liu, W. Sun, D. Liu, W. Li, Z. Li, K. Wang, T. Wang, *Interdiscip. Mater.* **2023**, *2*, 866.

[7] A. Classen, C. L. Chochos, L. Lüer, V. G. Gregoriou, J. Wortmann, A. Osvet, K. Forberich, I. McCulloch, T. Heumüller, C. J. Brabec, *Nat. Energy.* **2020**, *5*, 711.

[8] N. Gasparini, F. V. A. Camargo, S. Frühwald, T. Nagahara, A. Classen, S. Roland, A. Wadsworth, V. G. Gregoriou, C. L. Chochos, D. Neher, M. Salvador, D. Baran, I. McCulloch, A. Görling, L. Lüer, G. Cerullo, C. J. Brabec, *Nat. Commun.* **2021**, *12*, 1772.

[9] M. Azzouzi, N. P. Gallop, F. Eisner, J. Yan, X. Zheng, H. Cha, Q. He, Z. Fei, M. Heeney, A. A. Bakulin, J. Nelson, *Energy Environ. Sci.* **2022**, *15*, 1256.

[10] S. Karuthedath, J. Gorenflot, Y. Firdaus, N. Chaturvedi, C. S. P. D. Castro, G. T. Harrison, J. I. Khan, A. Markina, A. H. Balawi, T. A. D. Peña, W. Liu, R.-Z. Liang, A. Sharma, S. H. K. Paleti, W. Zhang, Y. Lin, E. Alarousu, S. Lopatin, D. H. Anjum, P. M. Beaujuge, S. D. Wolf, I. McCulloch, T. D. Anthopoulos, D. Baran, D. Andrienko, F. Laquai, *Nat. Mater.* **2021**, *20*, 378.

[11] Y. Fu, T. H. Lee, Y.-C. Chin, R. A. Pacalaj, C. Labanti, S. Y. Park, Y. Dong, H. W. Cho, J. Y. Kim, D. Minami, J. R. Durrant, J.-S. Kim, *Nat. Commun.* **2023**, *14*, 1870.

[12] H. Yan, S. Swaraj, C. Wang, I. Hwang, N. C. Greenham, C. Groves, H. Ade, C. R. McNeill, *Adv. Funct. Mater.* **2010**, *20*, 4329.

[13] K. Nakano, Y. Chen, B. Xiao, W. Han, J. Huang, H. Yoshida, E. Zhou, K. Tajima, *Nat. Commun.* **2019**, *10*, 2520.

[14] N. A. Ran, S. Roland, J. A. Love, V. Savikhin, C. J. Takacs, Y.-T. Fu, H. Li, V. Coropceanu, X. Liu, J.-L. Brédas, G. C. Bazan, M. F. Toney, D. Neher, T.-Q. Nguyen, *Nat. Commun.* **2017**, *8*, 79.

[15] C. Yan, S. Barlow, Z. Wang, H. Yan, A. K.-Y. Jen, S. R. Marder, X. Zhan, *Nat. Rev. Mater.* **2018**, *3*, 18003.

[16] J. Hou, O. Inganäs, R. H. Friend, F. Gao, *Nat. Mater.* **2018**, *17*, 119.

[17] Y. Firdaus, V. M. L. Corre, S. Karuthedath, W. Liu, A. Markina, W. Huang, S. Chattopadhyay, M. M. Nahid, M. I. Nugraha, Y. Lin, A. Seitkhan, A. Basu, W. Zhang, I. McCulloch, H. Ade, J. Labram, F. Laquai, D. Andrienko, L. J. A. Koster, T. D. Anthopoulos, *Nat. Commun.* **2020**, *11*, 5220.

[18] R. Yu, H. Yao, L. Hong, Y. Qin, J. Zhu, Y. Cui, S. Li, J. Hou, *Nat. Commun.* **2018**, *9*, 4645.

[19] C. Liu, Y. Fu, J. Zhou, L. Wang, C. Guo, J. Cheng, W. Sun, C. Chen, J. Zhou, D. Liu, W. Li, T. Wang, *Adv. Mater.* **2024**, *36*, 2308608.

[20] J. Wang, Y. Wang, P. Bi, Z. Chen, J. Qiao, J. Li, W. Wang, Z. Zheng, S. Zhang, X. Hao, J. Hou, *Adv. Mater.* **2023**, *35*, 2301583.

[21] R. Wang, Y. Jiang, W. Gruber, Y. He, M. Wu, P. Weitz, K. Zhang, L. Lüer, K. Forberich, T. Unruh, E. Spiecker, C. Deibel, N. Li, C. J. Brabec, *Adv. Mater. Interfaces.* **2022**, *9*, 2200342.

[22] R. Wang, L. Lüer, S. Langner, T. Heumueller, K. Forberich, H. Zhang, J. Hauch, N. Li, C. J. Brabec, *ChemSusChem.* **2021**, *14*, 3590.

[23] A. A. Bakulin, A. Rao, V. G. Pavelyev, P. H. M. van Loosdrecht, M. S. Pshenichnikov, D. Niedzialek, J. Cornil, D. Beljonne, R. H. Friend, *Science.* **2012**, *335*, 1340.

[24] D. Li, X. Zhang, D. Liu, T. Wang, *J. Mater. Chem. A.* **2020**, *8*, 15607.

[25] L. Lüer, R. Wang, C. Liu, H. Dube, T. Heumüller, J. Hauch, C. J. Brabec, *Adv. Sci.* **2023**, *11*, 2305948.

[26] X. Du, T. Heumueller, W. Gruber, O. Almora, A. Classen, J. Qu, F. He, T. Unruh, N. Li, C. J. Brabec, *Adv. Mater.* **2020**, *32*, 1908305.

[27] X. Du, L. Lüer, T. Heumueller, J. Wagner, C. Berger, T. Osterrieder, J. Wortmann, S. Langner, U. Vongsaysy, M. Bertrand, N. Li, T. Stubhan, J. Hauch, C. J. Brabec, *Joule.* **2021**, *5*, 495.

[28] C. Zhu, R. T. K. Kwok, J. W. Y. Lam, B. Z. Tang, *ACS Appl. Bio Mater.* **2018**, *1*, 1768.

[29] G. Chen, W. Li, T. Zhou, Q. Peng, D. Zhai, H. Li, W. Z. Yuan, Y. Zhang, B. Z. Tang, *Adv. Mater.* **2015**, *27*, 4496.

[30] Y. Liu, J. Zhao, Z. Li, C. Mu, W. Ma, H. Hu, K. Jiang, H. Lin, H. Ade, H. Yan, *Nat. Commun.* **2014**, *5*, 5293.

[31] L. Ye, X. Jiao, M. Zhou, S. Zhang, H. Yao, W. Zhao, A. Xia, H. Ade, J. Hou, *Adv. Mater.* **2015**, *27*, 6046.

[32] J. S. Wilson, N. Chawdhury, M. R. A. Al-Mandhary, M. Younus, M. S. Khan, P. R. Raithby, A. Köhler, R. H. Friend, *J. Am. Chem. Soc.* **2001**, *123*, 9412.

[33] S. Gadde, E. K. Batchelor, J. P. Weiss, Y. Ling, A. E. Kaifer, *J. Am. Chem. Soc.* **2008**, *130*, 17114.

[34] S. Ma, S. Du, G. Pan, S. Dai, B. Xu, W. Tian, *Aggregate.* **2021**, *2*, 96.

[35] Y.-C. Wei, S. F. Wang, Y. Hu, L.-S. Liao, D.-G. Chen, K.-H. Chang, C.-W. Wang, S.-H. Liu, W.-H. Chan, J.-L. Liao, W.-Y. Hung, T.-H. Wang, P.-T. Chen, H.-F. Hsu, Y. Chi, P.-T. Chou, *Nat. Photonics.* **2020**, *14*, 570.

[36] S. D. Dimitrov, B. C. Schroeder, C. B. Nielsen, Z. Fei, I. McCulloch, M. Heeney, J. R. Durrant, *Polymers.* **2016**, *8*, 14.

[37] Q. Guo, Y. Liu, M. Liu, H. Zhang, X. Qian, J. Yang, J. Wang, W. Xue, Q. Zhao, X. Xu, W. Ma, Z. Tang, Y. Li, Z. Bo, *Adv. Mater.* **2020**, *32*, 2003164.

[38] V. Coropceanu, X.-K. Chen, T. Wang, Z. Zheng, J.-L. Brédas, *Nat. Rev. Mater.* **2019**, *4*, 689.

[39] X.-K. Chen, V. Coropceanu, J.-L. Brédas, *Nat. Commun.* **2018**, *9*, 5295.

[40] J. Yuan, C. Zhang, B. Qiu, W. Liu, S. K. So, M. Mainville, M. Leclerc, S. Shoaee, D. Neher, Y. Zou, *Energy Environ. Sci.* **2022**, *15*, 2806.

[41] S.-U.-Z. Khan, J. Bertrandie, M. Gui, A. Sharma, W. Alsufyani, J. F. Gorenflot, F. Laquai, D. Baran, B. P. Rand, *Joule.* **2022**, *6*, 2821.

[42] N. R. Tummala, Z. Zheng, S. G. Aziz, V. Coropceanu, J.-L. Brédas, *J. Phys. Chem. Lett.* **2015**, *6*, 3657.

[43] T. Fritsch, J. Kurpiers, S. Roland, N. Tokmoldin, S. Shoaee, T. Ferron, B. A. Collins, S. Janietz, K. Vandewal, D. Neher, *Adv. Energy Mater.* **2022**, *12*, 2200641.

[44] J. Yan, E. Rezasoltani, M. Azzouzi, F. Eisner, J. Nelson, *Nat. Commun.* **2021**, *12*, 3642.

[45] M. S. Vezie, S. Few, I. Meager, G. Pieridou, B. Dörling, R. S. Ashraf, A. R. Goñi, H. Bronstein, I. McCulloch, S. C. Hayes, M. Campoy-Quiles, J. Nelson, *Nat. Mater.* **2016**, *15*, 746.

[46] C. Liu, L. Lüer, V. M. L. Corre, K. Forberich, P. Weitz, T. Heumüller, X. Du, J. Wortmann, J. Zhang, J. Wagner, L. Ying, J. Hauch, N. Li, C. J. Brabec, *Adv. Mater.* **2023**, 2300259.

[47] Y. Wang, J. Ren, Z. Shuai, *Nat. Commun.* **2023**, *14*, 5056.